# Improving Pixel-Based Change Detection Accuracy Using an Object-Based Approach in Multitemporal SAR Flood Images

Jun Lu, Jonathan Li, *Senior Member, IEEE*, Gang Chen, Linjun Zhao, Boli Xiong, *Member, IEEE*, and Gaoyao Kuang, *Member, IEEE*

*Abstract*—Most of existing change detection methods could be classified into three groups, the traditional pixel-based change detection (PBCD), the object-based change detection (OBCD), and the hybrid change detection (HCD). Nevertheless, both PBCD and OBCD have disadvantages, and classical HCD methods belong to intuitive decision-level fusion schemes of PBCD and OBCD. There is no optimum HCD method as of yet. Analyzing the complementarities of PBCD and OBCD method, we propose a new unsupervised algorithm-level fusion scheme (UAFS-HCD) in this paper to improve the accuracy of PBCD using spatial context information through: 1) getting the preliminary change mask with PBCD at first to estimate some parameters for OBCD; 2) deriving the unchanged area mask to eliminate the areas without changes, reducing error amplification phenomenon of OBCD; and 3) obtaining the final change mask by means of OBCD method. Taking flood detection with multitemporal SAR data as an example, we compared the new scheme with some classical methods, including PBCD, OBCD, and HCD method and supervised manual trial-and-error procedure (MTEP). The experimental results of flood detection showed that the new scheme was efficient and robust, and its accuracy sometimes can even exceed MTEP.

*Index Terms*—Change detection, object-based, pixel-based, SAR images, unsupervised change detection.

## I. INTRODUCTION

CHANGE detection is a process for identifying changes in a region by comparing its images taken at different times [1]. With the rapid increase of image spatial resolution and the expansion of the monitoring scope, the image change detection techniques are becoming increasingly important and difficult, especially for SAR images with the presence of speckle [2]–[5].

The process of change detection can be divided into preprocess and discrimination phase [6]. With different discrimination phases most of change detection methods may be divided into three initial groups: the traditional pixel-based change detection (PBCD), the object-based change detection (OBCD), and the hybrid change detection (HCD) [7], [8]. In addition, there were some complex approaches that incorporate more sophisticated algorithms, such as Markov random field [9]–[11], spectral clustering [12], or ensemble learning [13].

The discrimination process of PBCD consists of two steps [6]: deriving the difference image (DI) pixel by pixel, and segmenting DI to get the change mask. The first step is straightforward in change detection process, but the second step is still a classic problem [14]. Traditional PBCD methods are relatively simple, fast, and straightforward. In practice, PBCD methods are still the most commonly used methods for automated change detection [15], [16]. However, PBCD techniques only take individual pixels as their basic units without considering the spatial context [8]. Therefore, the accuracy of PBCD may be impaired and the problem becomes even worse due to image noise [14]. The results of PBCD strategies may often be limited when applied to very-high-resolution (VHR) imagery and SAR images [2], [17].

Unlike PBCD, OBCD techniques are based on image-objects, which are groups of pixels in the image and display meaningful objects in the scene [8]. OBCD methods need to extract the objects in the images and use the target objects to achieve the final change detection result [7]. The discrimination process of OBCD consists of deriving image-objects by segmenting the multitemporal images and comparing image-objects at different times. Recent studies have demonstrated that OBCD can provide improvements over PBCD especially when high spatial resolution imagery is used [18], [19]. Unfortunately, the performance of recent computer-aided segmentation algorithms was highly dependent on the specified task and no single algorithm was appropriate under all conditions [7]. Thus, a "trial-and-error" approach was typically used to optimize the parameters [20]. The existing automatic image classification and feature extraction techniques were not satisfied within the practical requirements of applications, and it is mandatory to invest further efforts to develop an effective automated solution [21].

Furthermore, there was an error amplification phenomenon with OBCD [6]. Since, the number of unchanged pixels is

often much larger than that of the changed pixels, if the feature extraction process is performed on the unchanged areas, the feature extraction error of each temporal image would be accumulated and amplified during the change detection process. This could result in false alarms. Image classification and feature extraction are time-consuming efforts and the parameter estimation of the extracted features is also expensive [22]. Therefore, feature extraction of the unchanged areas not only seriously affected the efficiency of the algorithm, but also obviously reduced its accuracy. Although PBCD can be found in some commercial software, while OBCD is still in the developing stage [23].

HCD refers to the use of two or more methods for change detection [7], [8], combining pixel-based, and object-based schemes. Some hybrid algorithms successfully reduced noisy changes, as well as the small and spurious changes introduced by the inconsistent delineation of objects [2], [24]. In [14], PBCD was used to identify changed pixels and followed by OBCD to determine the nature of changed pixels. In general, HCD methods combine PBCD with OBCD based on information fusion theory [25]–[29]. However, those HCD methods belong to an intuitive decision-level fusion scheme and usually the disadvantages of PBCD and OBCD both exist simultaneously. There is no so-called HCD method yet. Also, fully automated HCD methods are rare. Since multiple steps are involved in HCD, it remains uncertain how the final changes are affected by the combinations of pixel-based and object-based schemes [8].

Automated detection of flooded areas in SAR images automatically remains a very challenging task. Over the past decades, several studies used SAR data to map flood bodies with different techniques, but fully automated, time efficient, accurate, and stable flood extracting algorithms are scarce [30]. Recently, fully automated flood extraction algorithms, termed M1 and M2a [30], an enhanced version of M2a, termed M2b [31], have been proposed. In order to overcome the shortcomings of M2b when dealing with a nonbimodal histogram, an automated flood detection method M3 was proposed [32]. Both M2b and M3 are composed of the same sequence of steps, namely optimization of water distribution, thresholding, region growing, and change detection [32]. In fact, M2b falls into the OBCD method, whereas M3 falls into the HCD method. However, the performance of them is limited by the error amplification phenomenon and the image objects extracting process.

In this paper, we propose a totally different algorithm-level fusion framework based on the mutually complementary characteristics of PBCD and OBCD. There is no error amplification phenomenon within the unchanged areas. The detecting accuracy has been increased effectively using the spatial context information. Taking flood change detection with multitemporal SAR images as an example, we found out that the new unsupervised method is robust and sometimes even more accurate than the supervised manual trial-and-error procedure (MTEP).

This paper is organized as follows. Section II describes a new algorithm-level fusion scheme. In Section III, the new change detection framework is verified with simulated and real multitemporal SAR images, including a pair of Radarsat-1 SAR images and a pair of ERS-2 SAR images. Section IV concludes this paper and gives a prospect for future studies.

## II. METHODOLOGY

PBCD and OBCD are mutually complementary in three aspects. 1) The spatial context is often ignored by PBCD [33], but not by OBCD [34]. 2) PBCD is simple and fast. In contrast, OBCD is more complex and time-consuming due to image segmentation [35]. 3) The precision of PBCD depends on segmentation of DI, but the precision of the result with OBCD is independent with DI (most important). The precision of OBCD is mainly related to the accuracy of parameter estimation for image-objects extraction [36] and the error amplification phenomenon.

The goal of this study is to combine PBCD and OBCD to improve the performance of change detection. The basic idea is first to use a PBCD algorithm to estimate the parameters of image objects and label the unchanged areas, and then, an OBCD algorithm is adopted to produce a fine change detection mask based on the parameters and the unchanged areas estimated from the PBCD algorithms. This fusion scheme integrates PBCD and OBCD at the algorithm level. It is considerably different from the fusion at the decision-level, which usually directly integrates change detection results of PBCD and OBCD. Therefore, we can call this new HCD method as unsupervised algorithm-level fusion scheme (UAFS-HCD for short). In UAFS-HCD, the PBCD algorithm benefits from the OBCD algorithm with the regional spatial correlation information, whereas the OBCD algorithm benefits from the parameters of image objects and unchanged regions mask estimated by the PBCD algorithm. Fig. 1 shows the process diagram of UAFS-HCD.

The process of UAFS-HCD is divided into six parts: 1) inputting reference image and flood image; 2) PBCD; 3) estimating parameters of the image objects; 4) deriving unchanged area mask; 5) OBCD; and 6) outputting final change mask.

It is worth noting that our scheme is flexible and a large number of PBCD and OBCD methods can be included in this framework. Therefore, different change detection strategies with different demands of precision and efficiency can be customized within its usage. The details of the main process steps of UAFS-HCD are described below by taking flood detection with multitemporal SAR data as an example.

### A. Pixel-Based Change Detection

*1) Obtaining Difference Image:* This step is to simply generating DI using the multitemporal images through pixel by pixel comparison. For the registered multitemporal images, DI can be obtained by different approaches, such as image differencing, image ratio, or regression analysis [7]. If the input data are multispectral images, DI will form a spectral change vector [37]. If the resolutions of images are very high, a multiscale analysis method can be adopted [38].

For flood detection with multitemporal SAR images, a change detection measure based on the likelihood ratio and statistical properties of SAR images is well suited for change
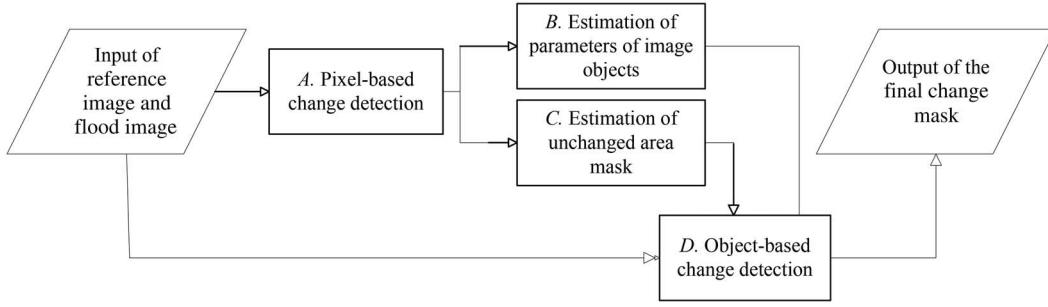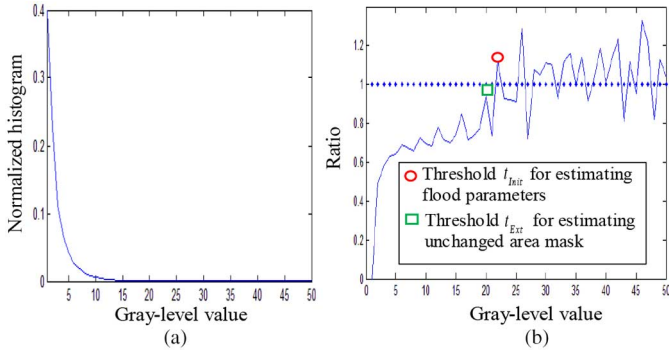
Fig. 1. Process diagram of our HCD scheme.



Fig. 2. Initial transition point $t_{Init}$ and the smaller transition point $t_{Ext}$ from simulated SAR images in Section III. (a) Local amplification of the normalized histogram of DI. (b) Ratio curve of the histogram of DI with $t_{Init}$ makred with a circle and $t_{Ext}$ marked with a rectangle.

detection [16]. With $F$ and $R$ representing the matrix of pixel values in the flood and reference images, respectively, the difference matrix $DI(i,j)$, according to DI, is defined as [16]

$$DI(i,j) = \frac{\sum_{(m,n)\in V_{ij}} R(m,n)}{\sum_{(m,n)\in V_{ij}} F(m,n)} + \frac{\sum_{(m,n)\in V_{ij}} F(m,n)}{\sum_{(m,n)\in V_{ij}} R(m,n)} \tag{1}$$

where $V$ defines the neighboring pixels of the pixel $(i,j)$, in a $w \times w$ window for reducing the effect of speckle noise (a typical value for $w$ is 3). Afterward, the value scope of $DI(i,j)$ is rescaled to the range of 0–255.

*2) Deriving Initial Change Mask:* There are numerous methods for segmenting DI, such as thresholding method, multiscale method, active contour model, and Markov random field techniques [39]–[42]. Among them, thresholding is very widely used. After all, there are only two classes in DI: changed parts and unchanged parts. The classic thresholding method aims to find the optimum threshold with the least errors in the resulting change detection [7].

For flood detection with multitemporal SAR images, the histogram of DI $h_{DI}(k)$ can be seen as a combination of a high peak area and an oscillating area. The high peak denotes the unchanged part, whereas the oscillating area represents the changed part (see Fig. 2). Therefore, the transition point between these two areas can be taken as the threshold to classify the changed and unchanged parts [16]. The ratio of the

histograms $r(k)$ at two adjacent gray levels can be used to find this transition point

$$r(k) = h_{DI}(k+1)/h_{DI}(k) \tag{2}$$

where $k \in [k_0, 255)$, and $k_0$ is the gray level according to the maximum value of $h_{DI}(k)$. For different threshold values with ranges from $k_0$ to 255, $r(k)$ is calculated accordingly. During the process, once $r(k)$ is larger than 1 [16], then let

$$t_{Init} = \{k | (r(k) \geq 1\} \tag{3}$$

where $t_{Init}$ is the transition point and it is just the initial threshold for DI. The initial mask of flood regions $M_{Init}$ is derived by thresholding DI with $t_{Init}$

$$M_{Init} = \begin{cases} 1, & DI(i,j) \geq t_{Init} \\ 0, & DI(i,j) < t_{Init}. \end{cases} \tag{4}$$

$M_{Init}$ can be used to estimate the parameters of image objects in the original images.

### B. Estimating Parameters of Image Objects

If the parameters of image objects are estimated correctly, it will be very easy and accurate to extract image objects for OBCD. In the initial change mask, the connected components may correspond to core areas of image objects, so it is a straightforward process to extract the pixels of image objects based on the mask of core image objects, thus making it feasible to calculate their parameters, such as statistic distribution and size. For example, image objects for flood detection with multitemporal SAR images are flooded areas. The initial change mask consists of several connected components, which directly correspond to the core water areas in the original flood image.

In fact, flood objects and the core water areas in the original SAR image have the same statistic properties. Backscatter intensity depends greatly on radar parameters (frequency, polarization, and incidence angle) and the geometric and electrical characteristics of the target [43]. Microwaves are generally rather well reflected by the water surface and do not almost penetrate into the water and the backscatter is mainly a function of the electrical properties and the surface roughness as compared to radar wavelength [44]. The dielectric constant of the water varies by temperature, salinity, and frequency

[45]. However, the dielectric constant of the water is relatively low for floods of freshwater, and the wind variation is not of extreme importance in generating surface roughness especially for longer wavelengths because surface roughness is too small to have much influence on backscatter at longer wavelengths. Therefore, for the most part, the scattering surface of flood is low, thus providing little backscatter and dark imagery [31]. On the other hand, the presence of suspended sediments in high concentration will not significantly influence the radar signal. Furthermore, the backscatter variability on a homogeneous surface is mainly due to speckle and in theory the probability distribution function (pdf) of backscatter originating from a homogeneous is a Gamma pdf [43].

Since flood objects in SAR flood image will keep the same Gamma pdf in theory, it is reasonable to estimate its pdf from the core water areas and to use the estimated pdf to finish the following OBCD process. It is worth noting that we do not need to choose the largest connected component from these core water areas for estimating the pdf of flood objects, because noise cannot dramatically affect the pdf of the flood objects.

More exactly, the pdf of flood objects in images can be estimated from $M_{Init}$ because $M_{Init}$ can provide most of the flooded pixels in the flood image. With $M_{Init}$, it is very easy and straightforward to extract the pixels in the flood image corresponding to $M_{Init} = 1$ and compute their histogram $h(l)$, which is the estimated pdf of flood objects, with $l$ representing the pixel values [either digital number (DN) or $\sigma^0$ in decibel, the radar reflectivity per unit area in ground range].

### C. Estimating Unchanged Area Mask

An unchanged area mask should be estimated before processing the OBCD step. Because of the error amplification phenomenon, any processing step of the OBCD within the unchanged areas is unnecessary, time wasting, and in fact harmful [6].

The unchanged area mask can be estimated by extending the initial change mask derived by PBCD. "Meaningless changes" and "real changes" are often mixed together in the global histogram. Even if the threshold is selected by MTEP [16], it would still bring some false and missed alarms. Obviously, to decrease missed alarms, a smaller threshold should be chosen. With the smaller threshold, DI is segmented and the unchanged area mask and extended change detection mask can be obtained simultaneously. The extended change mask ensures the missed alarm is lower than that of the initial change mask. Although in the extended mask, there are more false alarms than that of the initial change mask, which could be removed by the subsequent OBCD procedure by using the spatial context information.

For flood detection with multitemporal SAR images, the transition point in (3) is chosen to separate the high peak and the oscillating area of the histogram of DI into the changed and unchanged parts [16]. In fact, the high peak is composed of a more abrupt high peak and some oscillating parts, which belong to changed parts. Therefore, in order to derive the unchanged area mask, the most obvious oscillating part, which belongs to

changed parts, can be used to find a small transition point than $t_{Init}$ in (3)

$$t_{Ext} = \{k| \max(r(k)),\ k_0 < k < t_{Init}\} \qquad (5)$$

where $t_{Ext}$ is the smaller transition point.

Some figures from the simulated SAR images in Section III were presented here to illustrate how to find the smaller transition point $t_{Ext}$. Fig. 2(a) shows the local amplification of the normalized histogram of DI, and Fig. 2(b) shows its ratio curve calculated by (2). The initial transition point $t_{Init}$ marked with a circle in Fig. 2(b) surely separates the high peak from the changed parts, but this high peak still has a long tail containing some oscillating areas which belong to the changed parts. Among these oscillating parts, the most obvious oscillating part is the most important one and must not be ignored. Therefore, a small transition point $t_{Ext}$ is chosen by (5) to greatly retain the real changes. In Fig. 2(b), we mark the small transition point $t_{Ext}$ with a rectangle. The extended flood mask of water regions $M_{Ext}$ is derived by thresholding DI with $t_{Ext}$

$$M_{Ext} = \begin{cases} 1, & DI(i,j) \geq t_{Ext} \\ 0, & DI(i,j) < t_{Ext}. \end{cases} \qquad (6)$$

The unchanged area mask $\bar{M}_{Ext}$ is the logical inverter of $M_{Ext}$

$$\bar{M}_{Ext} = \begin{cases} 1, & \text{if } M_{Ext} = 0 \\ 0, & \text{if } M_{Ext} = 1. \end{cases} \qquad (7)$$

Obviously, $M_{Ext}$ has a smaller under-detection rate and a larger over-detection rate than that of $M_{Init}$. The next OBCD process will be done within $M_{Ext}$ and try to suppress the over-detection rate using spatial-contextual information. It is worth noting that within the unchanged area mask there is no error amplification phenomenon any longer. That is to say, spatial contextual information can be used successfully with error amplification phenomenon being suppressed simultaneously.

### D. Object-Based Change Detection

*1) Obtaining the Image Objects:* In UAFS-HCD, the OBCD procedure differs from the classic OBCD in two aspects. 1) The feature extraction is only performed within the areas labeled by the extended mask $M_{Ext}$, and it not only significantly saves the processing time, but also avoids the error amplification phenomenon in the unchanged areas. 2) Since the parameters have derived from the PBCD procedure, there is no need to estimate the parameters of image objects with any trial-and-error approach.

A flooding area in SAR images is a connected region with similar low gray values. Therefore, the water mask $M_{Flood}$ in the flood image can be derived from region growing [46] in the flood image within $M_{Ext}$. Two procedures are required to accomplish this process and we can use the parameters estimated previously.

1) First, the seeds of "open water" in the flood image should be extracted. This procedure is similar to the algorithm in [32]. The abscissa value corresponding to the mode of $h(l)$ can be selected as the threshold, with which the flood image is thresholded to get the seeds of "open water" [32]. For UAFS-HCD, the main difference is that all the seeds from outside $M_{Ext}$ or inside the unchanged area mask $\bar{M}_{Ext}$ will be eliminated, which can save the processing time and reduce the over-detection rate at the same time.

2) Second, the seeds of water areas in the flood image are dilated using the region growing approach [46] until an optimal tolerance level is reached. Obviously, the optimal tolerance level will provide the maximal similarity between $h(l)$ and the histogram of water regions after region growing which can be denoted by $\hat{h}(l)$. Therefore, the optimal tolerance level can be derived by calculating similarity measure between $h(l)$ and $\hat{h}(l)$. Since $h(l)$ and $\hat{h}(l)$ are one-dimensional (1-D) histograms, Kullback–Leibler (KL) distance [47] is very fit for calculating similarity measure between them

$$\kappa(h,\ \hat{h}) = \sum_l h(l) \log \frac{h(l)}{\hat{h}(l)} \qquad (8)$$

where $\kappa(h,\ \hat{h})$ is KL distance, $h(l)$ is the estimated pdf of flood values in flood image, $\hat{h}(l)$ is the histogram of water regions after region growing in flood image, and $l$ represents the pixel values (either DN or $\sigma^0$ in decibel). If the tolerance level for region growing is too small or too large, $h(l)$ and $\hat{h}(l)$ will be very different, so the KL distance will be a very large positive value. For the optimal tolerance level, $h(l)$ and $\hat{h}(l)$ are very similar, so the KL distance will be very close to zero. Therefore, the lowest value of KL distance corresponds to the nearest distance between $\hat{h}(l)$ and $h(l)$, and also corresponds to the optimal tolerance level. With the optimal tolerance level, the mask of flood areas $M_{Flood}$ is derived by region growing in the flood image [32].

*2) Detecting Changes:* With classified image objects, change detection can produce straightforward results by comparing the image objects before and after change. It is worth mentioning that error propagation in UAFS-HCD has been reduced due to using the unchanged area mask.

For flood detection with multitemporal SAR images, the mask of permanent water bodies $M_{Ref}$ in the reference image can be derived by region growing with the same unchanged area mask and the same parameters as before, such as the threshold for deriving seeds and the optimal tolerance level for region growing. Finally, the final flood mask will be derived by removing the mask of permanent water from the computed flood extent in the flood image [32]

$$M_{Final} = M_{Flood} - M_{Ref}. \qquad (9)$$

In UAFS-HCD, PBCD provides the exact parameters of image objects and the unchanged mask for OBCD, whereas OBCD can give the final change mask by using spatial contextual information. There is no error amplification phenomenon in the area labeled by the unchanged mask and the "trial-and-error" approach for optimizing the parameters of image objects is unnecessary. Therefore, it is reasonable for UAFS-HCD to provide more accurate results robustly and efficiently, which will be verified in the next section with simulated and real multitemporal SAR images.

## III. RESULTS AND DISCUSSION

Some PBCD, OBCD, and HCD algorithms proposed recently have been used here to assess the capability of the proposed UAFS-HCD approach. Specifically, the flood extent results are compared with those of the other four methods: the supervised MTEP [16] based on a log-ratio detector and the analysis of the DI, which consists of finding the threshold value that minimizes the overall errors; the change detection threshold selection method based on the histogram ratio (donated by "Xiong algorithm") [16]; the M2b method [31]; and the M3 method [32]. As discussed in Section I, M2b [31] belongs to the OBCD methods, M3 [32], in fact, is a HCD algorithm, Xiong algorithm and MTEP [16] both are PBCD methods, and only MTEP [16] is a supervised method. All of the parameters used in UAFS-HCD were optimized automatically.

The number of over-detected pixels (OP), the number of under-detected pixels (UP), and overall errors (OE) are adopted to evaluate the three methods.

Some simulated data sets and real SAR data sets acquired by distinct sensors have been chosen to validate the effectiveness of the proposed approach including a pair of Radarsat-1 SAR images [32] and a pair of ERS-2 SAR images [16].

### A. Simulated Images

We first tested our scheme using simulated images in order to objectively assess the performances in a controlled environment. The ground truth image ($500 \times 500$ pixels) is shown in Fig. 3(c), in which two different backscatter intensities are chosen, one relatively bright ($\sigma^0$ is $-10$ dB) for the background and one relatively dark ($\sigma^0$ is $-22$ dB) for the six round flood objects. The ground truth image and the background image were degraded by speckle noise that satisfies a Gamma distribution [48] to derive the simulated image pairs, the flood image and the reference image, respectively. Several simulated image pairs with different noise levels measured by equivalent number of looks (ENL) [49] were used to feed these algorithms.

At first, we compared the proposed method with the other algorithms on one simulated image pair (ENL = 5). Fig. 3(a) and (b) shows the flood image and the reference image when ENL = 5. The results obtained from the various methods are listed in Table I and shown in Fig. 3(d), (e), (g), and (h), respectively.

Fig. 3(i) shows the ratio curve of the histogram of DI and two important thresholds used in the proposed algorithm for estimating flood parameters and for estimating unchanged area mask. Fig. 3(h) suggests that the proposed method can generate accurate results, which is also confirmed by Table I. The proposed method is characterized by 24 over-detected pixels and
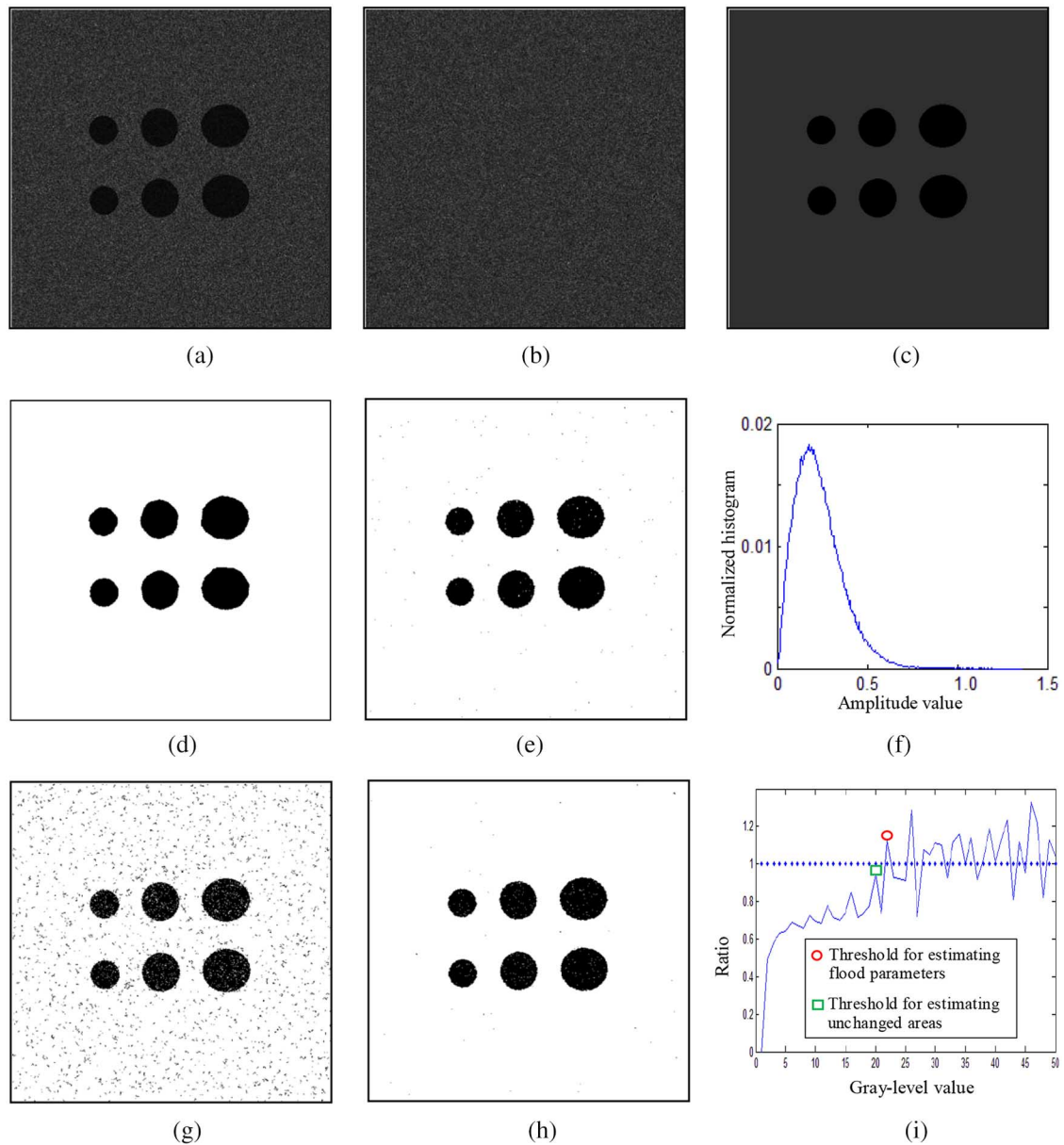
Fig. 3. Simulated images and results (the black pixels show the detected floods): (a) Flood image. (b) Reference image. (c) Ground truth. (d) Change detection map with MTEP [16]. (e) Change detection map with Xiong algorithm [16]. (f) Histogram of flood image, which is not bimodal; therefore, the assumption of M2b does not hold [31]. (g) Change detection map with M3 [32]. (h) Change detection map with the proposed method. (i) Ratio curve of the histogram of DI (the threshold for estimating flood parameters and the threshold for estimating unchanged area mask are marked with a circle and a rectangle, respectively).

TABLE I
EVALUATION OF FLOOD EXTENT RESULTS (SIMULATED SAR IMAGES)

| Method | OP | UP | OE |
|---|---|---|---|
| MTEP (16) | 185 | 220 | 405 |
| Xiong algorithm (16) | 46 | 898 | 944 |
| M2b (31) | – | – | – |
| M3 (32) | 3066 | 814 | 3880 |
| Proposed Method | 24 | 696 | 720 |

OP, the number of over-detected pixels; UP, the number of under-detected pixels; OE, the number of overall errors.

696 under-detected pixels (with 720 total errors, i.e., a 0.288% total error detection rate), which is very similar to MTEP, the only supervised manual method, with 185 over-detected pixels and 220 under-detected pixels.

Comparing the proposed method with the Xiong algorithm, a PBCD method, we can see the under-detected flood pixels decreased from 898 with Xiong algorithm to 696 with the proposed method and the over-detected flood pixels also decreased from 46 with the Xiong algorithm to 24 with the proposed method.

The M2b method is based on the assumption that a flood image contains a relatively high number of pixels with low backscatter values, exhibiting a bimodal histogram. Since, in this case, the histogram of the flood image is not bimodal, as shown in Fig. 3(f), the assumption of M2b method does not hold any more. Obviously OBCD algorithms cannot provide accurate results robustly when some assumptions do not hold, whereas the proposed method is a very robust algorithm without any assumption on the histogram of the flood image.
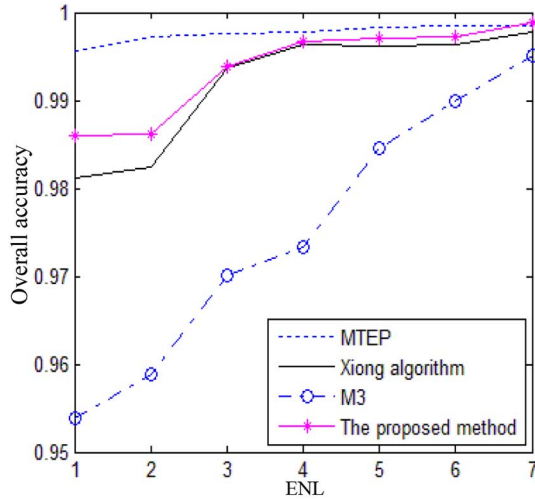
Fig. 4. Overall accuracy as a function of noise level measured by ENL.

M3, a kind of HCD method, has 3880 over-detected pixels in this case that is mainly due to the error amplification phenomenon. With the help of the unchanged area mask, the number of over-detection pixels for the proposed method has a sharp decrease.

Furthermore, in order to examine the robustness of different methods to noise levels, several simulated image pairs with different ENL ranging from 1 to 7 were generated independently and the overall accuracy for quantitative evaluation was adopted. The overall accuracy is calculated as the ratio between the number of pixels that are correctly detected and the total number of pixels. Fig. 4 shows the overall accuracy as a function of noise level measured by ENL.

As we can see, the curve of the proposed method is generally above the curve of the Xiong algorithm at different noise level, which means the proposed algorithm can robustly improve PBCD accuracy using spatial context information.

M3 tends to be affected by speckle noise more easily and the curve drops more quickly with the increasing of noise level, which was also due to the error amplification phenomenon. Comparatively, the proposed method achieved relatively robust results with an unchanged area mask, which suppressed the error amplification phenomenon effectively.

Fig. 4 suggests that the overall accuracy of the proposed method is above all the unsupervised methods at different noise level. More surprisingly, when $ENL = 7$ the proposed method even overcame MTEP, the supervised manual method. It is worth noting that it is impossible for the Xiong algorithm to overcome MTEP.

### B. Radarsat-1 SAR Images

Fig. 5(a) and (b) shows a pair of real multitemporal SAR data set made up of two image (C-band and HH polarization), which are acquired by Radarsat-1 SAR sensor over some lakes near the city of Ottawa, Canada, in July and August 1997, respectively [50]. The flooding event caused a rise in the surface of lakes, leading to changes in their areas. The ENL of

the two images computed according to [51] is 12.5 and 12.6, respectively. The available ground truth shown in Fig. 5(c) was obtained by integrating prior information with photograph interpretation [32].

The quantitative and qualitative change detection results obtained from different methods in this case are listed in Table II and shown in Fig. 5(d)–(h), respectively. Fig. 5(i) shows the ratio curve of the histogram of DI. The thresholds for estimating flood parameters and for estimating unchanged area mask are also marked in Fig. 5(i).

Based on Fig. 5, we can observe that the change detection results obtained from the proposed method are very similar to that of MTEP. As shown in Table II, the best result obtained is given by the MTEP method and is characterized by 1222 over-detected pixels and 1912 under-detected pixels. The performance of the proposed method is pretty good with 797 over-detected pixels and 2726 under-detected pixels (with 3523 total errors, i.e., a 3.48% total error detection rate), which is better than that of Xiong algorithm with 3292 under-detected flood pixels and 665 over-detected pixels.

M2b had the worst result (with 6625 overall errors), which is due to the fact that it is very difficult to extract the image objects accurately and automatically from the original SAR images without enough information about the image objects.

M3 derived a better result than M2b, but it had 1793 over-detected pixels in this case which was mainly due to the error amplification phenomenon. With the help of the unchanged area mask, the number of over-detection pixels for the proposed method had a sharp decrease.

Among the unsupervised methods, the proposed method derives the best result in accuracy, especially for the percentage of over-detected flood pixels which decrease to some extent.

### C. ERS-2 SAR Data Set

Fig. 6(a) and (b) shows a pair of real multitemporal SAR data set made up of two C-band SAR images acquired by ERS-2 before and after floods over the city of Bern, Switzerland on April 20 and May 25, 1999, respectively. The pixel size of the images is about 12.5 m. The ENL of the two images considered is 10.89 and 9.26, respectively [50]. Fig. 6(c) shows the ground truth of the change detection map that is manually created with a visual interpretation [16]. Fig. 6(d) and (f)–(h) shows the change detection maps achieved by MTEP, Xiong algorithm, M3, and the proposed method, respectively. Fig. 6(i) shows the local amplification of ratio curve from the histogram of DI with two marked thresholds. The results are also tabulated in Table III.

As shown in Fig. 6 and Table III, the proposed method obtained the best result and is characterized by 64 over-detected pixels, 322 under-detected pixels, and 386 overall errors (i.e., a 0.30% total error detection rate). The Xiong algorithm produced more errors (428 overall errors). The M2b method failed in this case since the histogram of the flood image is not bimodal, as shown in Fig. 6(f), and the assumption of the
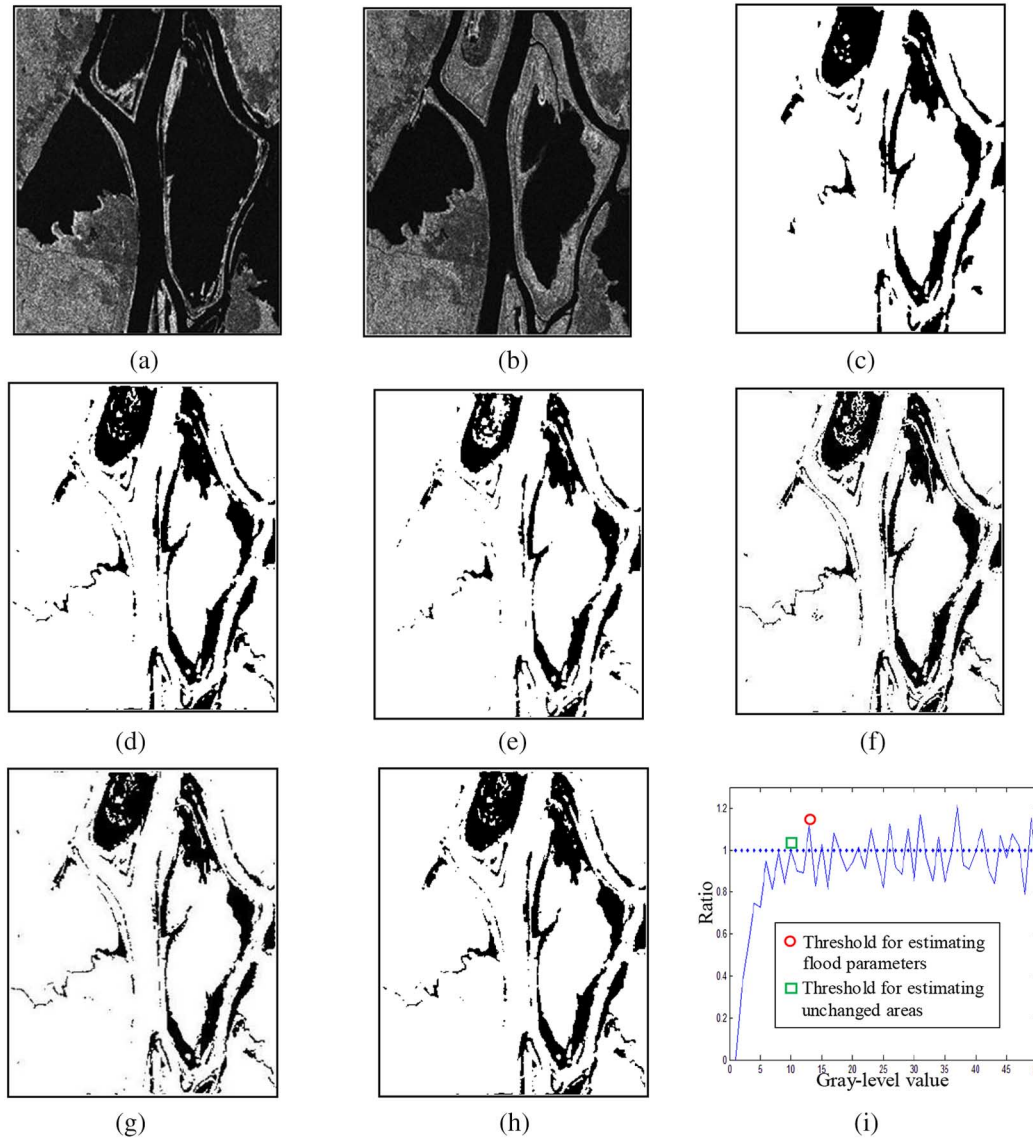
Fig. 5. Radarsat-1 SAR images and results (the black pixels show the detected floods): (a) Flood image. (b) Reference image. (c) Ground truth. (d) Change detection map with MTEP [16]. (e) Change detection map with Xiong algorithm [16]. (f) Change detection map with M2b [31]. (g) Change detection map with M3 [32]. (h) Change detection map with the proposed method. (i) Ratio curve of the histogram of DI (the threshold for estimating flood parameters and the threshold for estimating unchanged area mask are marked with a circle and a rectangle, respectively).

TABLE II
EVALUATION OF FLOOD EXTENT RESULTS (RADARSAT-1 IMAGES)

| Method | OP | UP | OE |
|---|---|---|---|
| MTEP (16) | 1222 | 1912 | 3134 |
| Xiong algorithm (16) | 665 | 3292 | 3957 |
| M2b (31) | 1104 | 5521 | 6625 |
| M3 (32) | 1793 | 2847 | 4640 |
| Proposed method | 797 | 2726 | 3523 |

OP, the number of over-detected pixels; UP, the number of under-detected pixels; OE, the number of overall errors.

TABLE III
EVALUATION OF FLOOD EXTENT RESULTS (ERS-2 IMAGES)

| Method | OP | UP | OE |
|---|---|---|---|
| MTEP (16) | 140 | 272 | 412 |
| Xiong algorithm (16) | 111 | 317 | 428 |
| M2b (31) | – | – | – |
| M3 (32) | 464 | 155 | 619 |
| Proposed method | 64 | 322 | 386 |

OP, the number of over-detected pixels; UP, the number of under-detected pixels; OE, the number of overall errors.

M2b method does not hold any longer. Comparing the proposed method with M3 [see Fig. 6(g)], one can find the number of under-detected pixels decreases abruptly from 464 with M3 to 64 with the proposed method due to the using of the unchanged area mask.

It is worth noting that in this specific case the proposed method is even better than MTEP (with 412 overall errors), the supervised manual method. It is reasonable because the proposed method can use the spatial context information but MTEP method cannot.
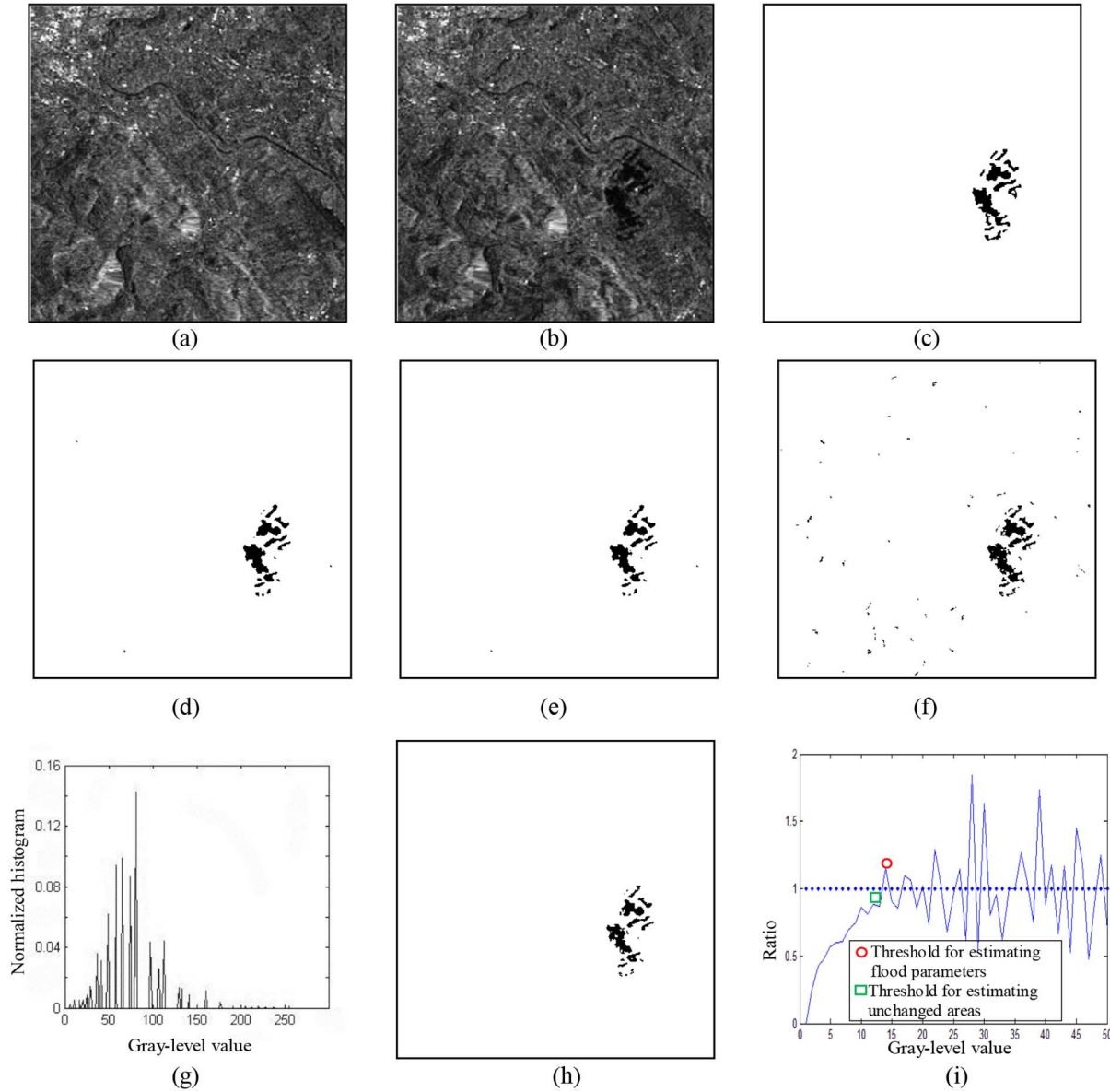
Fig. 6. ERS-2 SAR images and results (the black pixels show the detected floods): (a) and (b) ERS-2SAR images of Bern, Switzerland before and after floods. (c) ground truth. (d) Change detection map with MTEP [16]. (e) Change detection map with the Xiong algorithm [16]. (f) Histogram of flood image, which is not bimodal; therefore, the assumption of M2b does not hold [31]. (g) Change detection map with M3 [32]. (h) Change detection map with the proposed method. (i) Ratio curve of the histogram of DI (the threshold for estimating flood parameters and the threshold for estimating unchanged area mask are marked with a circle and a rectangle, respectively).

## IV. CONCLUSION

This paper has presented a new unsupervised algorithm-level fusion scheme for change detection (UAFS-HCD). In this scheme, OBCD was used to improve the accuracy of PBCD algorithms. On the other hand, PBCD helps to remove the areas without any change and provides the estimated parameters for extracting image objects. With the estimated parameters and the unchanged area mask, OBCD can help to improve the accuracy by using the neighborhood information. There is no error amplification phenomenon within the unchanged area mask and the over-detection rate is suppressed effectively. The new scheme takes the advantages of both PBCD and OBCD, and makes up their own deficiencies at the same time. Using floods monitoring as an example, we validated

the effectiveness of the new scheme UAFS-HCD with simulated SAR image sets at different noise level and two pairs of real multitemporal SAR image sets. It is possible for the proposed method to derive even more accurate result than MTEP, the supervised manual method (PBCD method). In all of these cases, the proposed method is more accurate, and robust than the Xiong algorithm (PBCD method), M2b (OBCD method), and M3 (HCD method). In addition, the proposed algorithm is more efficient than M2b and M3 because there is no time-consuming optimization of flood distribution and the seeds within the unchanged area mask are eliminated before region growing.

There is still some work to do, such as analyzing the sensitivity of the image registration error in the new scheme and

adapting combinations of different methods from PBCD and OBCD in various change detection applications.

## ACKNOWLEDGMENT

## REFERENCES

[1] R. J. Radke, S. Andra, O. Al-Kofahi, and B. Roysam, "Image change detection algorithms: A systematic survey," *IEEE Trans. Image Process.*, vol. 14, no. 3, pp. 294–307, Mar. 2005.

[2] S. Hachicha and F. Chaabane, "Comparison of change detection indicators in SAR images," in *Proc. 8th Eur. Conf. Synth. Aperture Radar*, 2010, pp. 109–112.

[3] S. M. Scarborough *et al.*, "A challenge problem for SAR change detection and data compression," *Proc. SPIE*, vol. 7699, p. 76990U, 2010.

[4] P. Gamba, F. Dell'Acqua, and G. Lisini, "Change detection of multitemporal SAR data in urban areas combining feature-based and pixel-based techniques," *IEEE Trans. Geosci. Remote Sens.*, vol. 44, no. 10, pp. 2820–2827, Oct. 2006.

[5] B. Aiazzi, L. Alparone, S. Baronti, A. Garzelli, and C. Zoppetti, "Nonparametric change detection in multitemporal SAR images based on mean-shift clustering," *IEEE Trans. Geosci. Remote Sens.*, vol. 51, no. 4, pp. 2022–2031, Apr. 2013.

[6] D. Lu, P. Mausel, E. Brondízio, and E. Moran, "Change detection techniques," *Int. J. Remote Sens.*, vol. 25, no. 12, pp. 2365–2407, Jun. 2004.

[7] M. Hussain, D. Chen, A. Cheng, H. Wei, and D. Stanley, "Change detection from remotely sensed images: From pixel-based to object-based approaches," *ISPRS J. Photogramm. Remote Sens.*, vol. 80, pp. 91–106, 2013.

[8] G. Chen, G. Hay, L. M. T. Carvalho, and M. A. Wulder, "Object-based change detection," *Int. J. Remote Sens.*, vol. 33, no. 14, pp. 4434–4457, 2012.

[9] F. Baselice, G. Ferraioli, and V. Pascazio, "Markovian change detection of urban areas using very high resolution complex SAR images," *IEEE Geosci. Remote Sens. Lett.*, vol. 11, no. 5, pp. 995–999, May 2014.

[10] G. Moser and S. B. Serpico, "Unsupervised change detection from multi-channel SAR data by Markovian data fusion," *IEEE Geosci. Remote Sens. Lett.*, vol. 47, no. 7, pp. 2114–2128, Jul. 2009.

[11] T. Kasetkasem and P. K. Varshney, "An image change detection algorithm based on Markov random field models," *IEEE Trans. Geosci. Remote Sens.*, vol. 40, no. 8, pp. 1815–1823, Aug. 2002.

[12] X. Zhang, L. Jiao, F. Liu, and L. Bo, "Spectral clustering ensemble applied to SAR image segmentation," *IEEE Trans. Geosci. Remote Sens.*, vol. 46, no. 7, pp. 2126–2136, Jul. 2008.

[13] B. W. Martin and R. R. Vatsavai, "Image change detection via ensemble learning," in *Proc. SPIE Algorithms Technol. Multispectral Hyperspectral Ultraspectral Imagery XIX*, Baltimore, MD, USA, 2013, vol. 8743, p. 874305.

[14] Z. Ghofrani, M. Mokhtarzade, M. R. Sahebi, and A. Beykikhoshk, "Evaluating coverage changes in national parks using a hybrid change detection algorithm and remote sensing," *J. Appl. Remote Sens.*, vol. 8, no. 1, p. 083646(1–16), 2014.

[15] R. Fraser, I. Olthof, and D. Pouliot, "Monitoring land cover change and ecological integrity in Canada's national parks," *Remote Sens. Environ.*, vol. 113, pp. 1397–1409, Jul. 2009.

[16] B. Xiong, J. M. Chen, and G. Kuang, "A change detection measure based on a likelihood ratio and the statistical properties of SAR intensity images," *Remote Sens. Lett.*, vol. 3, no. 3, pp. 267–275, 2012.

[17] I. Niemeyer and M. J. Canty, "Pixel-based and object-oriented change detection analysis using high-resolution imagery," in *Proc. 25th Symp. Safeguards Nucl. Mater. Manage.*, 2003, pp. 13–15.

[18] T. Blaschke, "Object based image analysis for remote sensing," *ISPRS J. Photogramm. Remote Sens.*, vol. 65, no. 1, pp. 2–16, 2010.

[19] C. Huo, Z. Zhou, H. Lu, C. Pan, and K. Chen, "Fast object-level change detection for VHR images," *IEEE Geosci. Remote Sens. Lett.*, vol. 7, no. 1, pp. 118–122, Jan. 2010.

[20] S. Roostaei, S. A. Alavi, M. R. Nikjoo, and K. V. Kamran, "Evaluation of object-oriented and pixel based classification methods for extracting changes in urban area," *Int. J. Geomatics Geosci.*, vol. 2, no. 3, pp. 738–749, 2012.

[21] P. Lu, A. Stumpf, N. Kerle, and N. Casagli, "Object-oriented change detection for landslide rapid mapping," *IEEE Geosci. Remote Sens. Lett.*, vol. 8, no. 4, pp. 701–705, Jul. 2011.

[22] P. Hofmann, P. Lohmann, and S. Müller, "Change detection by object-based change indications," in *Proc. 4th EARSeL Workshop Remote Sens. Develop. Countries Conjunction GISDECO*, Jun. 2008, vol. 8, pp. 4–7.

[23] P. Gamba, F. Dell'Acqua, and G. Lisini, "Change detection of multitemporal SAR data in urban areas combining feature-based and pixel-based techniques," *IEEE Trans. Geosci. Remote Sens.*, vol. 44, no. 10, pp. 2820–2827, Oct. 2006.

[24] D. Carvalho, L. M. Tavares, J. G. P. W. Clevers, S. M. D. Jong, and A. K. Skidmore, "Forestry database updating based on remote sensing change detection," in *Proc. Anais XII Simpos. Brasil. Sensoriamento Remoto*, Apr. 2005, pp. 465–472.

[25] J. Aguirre-Gutiérrez, A. C. Seijmonsbergen, and J. F. Duivenvoorden, "Optimizing land cover classification accuracy for change detection, a combined pixel-based and object-based approach in a mountainous area in Mexico," *Appl. Geogr.*, vol. 34, pp. 29–37, 2012.

[26] P. Gamba, F. Dell'Acqua, and G. Lisini, "Change detection of multitemporal SAR data in urban areas combining feature-based and pixel-based techniques," *IEEE Trans. Geosci. Remote Sens.*, vol. 44, no. 10, pp. 2820–2827, Oct. 2006.

[27] F. Bovolo, C. Marin, and L. Bruzzone, "A multilevel approach to change detection for port surveillance with very high resolution SAR images," in *Proc. 6th Int. Workshop Anal. Multi-Temp. Remote Sens. Images (Multitemp'11)*, Trento, Italy, Jul. 12–14, 2011, pp. 9–12.

[28] L. Bruzzone and F. Melgani, "A data fusion approach to unsupervised change detection," in *Proc. IEEE Int. Conf. Geosci. Remote Sens. Symp. (IGARSS'03)*, Toulouse, France, 2003, vol. 2, pp. 1374–1376.

[29] F. Bovolo and L. Bruzzone, "A theoretical framework for unsupervised change detection based on change vector analysis in polar domain," *IEEE Trans. Geosci. Remote Sens.*, vol. 45, no. 1, pp. 218–236, Jan. 2007.

[30] P. Matgen, R. Hostache, G. J.-P. Schumann, L. Hoffmann, and H. H. G. Savenjie, "Towards an automated SAR-based flood monitoring system: Lessons learned from two case studies," *Phys. Chem. Earth*, vol. 36, no. 7–8, pp. 241–252, 2011.

[31] L. Giustarini *et al.*, "A change detection approach to flood mapping in urban areas using TerraSAR-X," *IEEE Trans. Geosci. Remote Sens.*, vol. 51, no. 4, pp. 2417–2430, Apr. 2013.

[32] J. Lu *et al.*, "Automated flood detection with improved robustness and efficiency using multi-temporal SAR data," *Remote Sens. Lett.*, vol. 5, no. 3, pp. 240–248, 2014.

[33] R. Radke, S. Andra, O. Al-Kofahi, and B. Roysam, "Image change detection algorithms: A systematic survey," *IEEE Trans. Image Process.*, vol. 14, no. 3, pp. 294–307, Mar. 2005.

[34] V. Walter, "Object-based classification of remote sensing data for change detection," *ISPRS J. Photogramm. Remote Sens.*, vol. 58, pp. 225–238, 2004.

[35] I. Lizarazo and P. Elsner, "From pixels to grixels: A unified functional model for geographic object-based image analysis," in *Proc. Pixels Objects Intell. Geogr. Object Based Image Anal. 21st Century (GEOBIA0'08)*, 2008, vol. XXXVIII-4/C1, pp. 1682–1777.

[36] B. Thomas and J. Strobl, "What's wrong with pixels? Some recent developments interfacing remote sensing and GIS," *GeoBIT/GIS*, vol. 6, no. 1, pp. 12–17, 2001.

[37] F. Bovolo, L. Bruzzone, and M. Marconcini, "A novel approach to unsupervised change detection based on a semisupervised SVM and a similarity measure," *IEEE Trans. Geosci. Remote Sens.*, vol. 46, no. 7, pp. 2070–2082, Jul. 2008.

[38] F. Bovolo and L. Bruzzone, "A detail-preserving scale-driven approach to unsupervised change detection in multitemporal SAR images," *IEEE Trans. Geosci. Remote Sens.*, vol. 43, no. 12, pp. 2963–2972, Dec. 2005.

[39] P. Coppin, I. Jonckheere, K. Nackaerts, and B. Muys, "Digital change detection methods in ecosystem monitoring: A review," *Int. J. Remote Sens.*, vol. 25, no. 9, pp. 1565–1596, 2004.

[40] T. Celik and K.-K. Ma, "Multitemporal image change detection using undecimated discrete wavelet transform and active contours," *IEEE Trans. Geosci. Remote Sens.*, vol. 49, no. 2, pp. 706–716, Feb. 2011.

[41] L. M. T. Carvalho, L. M. G. Fonseca, F. Murtagh, and J. G. P. W. Clevers, "Digital change detection with the aid of multi-resolution wavelet analysis," *Int. J. Remote Sens.*, vol. 22, no. 18, pp. 3871–3876, 2001.

[42] S. Sara and M. J. V. Zoej, "Unsupervised change detection based on improved Markov random field technique using multichannel synthetic aperture radar images," *J. Appl. Remote Sens.*, vol. 8, no. 1, p. 083591, 2014.

[43] D. C. Mason *et al.*, "Flood detection in urban areas using TerraSAR-X," *IEEE Trans. Geosci. Remote Sens.*, vol. 48, no. 2, pp. 882–894, Feb. 2010.

[44] P. Clemente-Colón and X.-H. Yan, "Observations of East Coast upwelling conditions in synthetic aperture radar imagery," *IEEE Trans. Geosci. Remote Sens.*, vol. 37, no. 5, pp. 2239–2248, Sep. 1999.

[45] B. Holt, C. R. Jackson, and J. R. Apel, *Synthetic Aperture Radar Marine User's Manual*. Washington, DC, USA: National Oceanic and Atmospheric Administration, 2004, pp. 263–275 [Online]. Available: http://www.sarusersmanual.com, accessed on 24 Oct. 2013

[46] R. C. Gonzales and R. E. Woods, *Digital Image Processing*. Englewood Cliffs, NJ, USA: Prentice Hall, 2002.

[47] S. Kullback and R. A. Leibler, "On information and sufficiency," *Ann. Math. Statist.*, vol. 22, no. 1, pp. 79–86, 1951.

[48] X. Hua, L. E. Pierce, and F. T. Ulaby, "Despeckling SAR images using a low-complexity wavelet denoising process," in *Proc. IEEE Int. Conf. Geosci. Remote Sens. Symp. (IGARSS'02)*, Toronto, ON, Canada, 2002, pp. 321–324.

[49] C. Oliver and S. Quegan, *Understanding Synthetic Aperture Radar Images*. Norwood, MA, USA: Artech House, 1998.

[50] M. Gong, Z. Zhou, and J. Ma, "Change detection in synthetic aperture radar images based on image fusion and fuzzy clustering," *IEEE Trans. Image Process.*, vol. 21, no. 4, pp. 2141–2151, Apr. 2012.

[51] Y. Bazi, L. Bruzzone, and F. Melgani, "An unsupervised approach based on the generalized Gaussian model to automatic change detection in multitemporal SAR images," *IEEE Trans. Geosci. Remote Sens.*, vol. 43, no. 4, pp. 874–887, Apr. 2005.

**Jun Lu** received the B.S. degree in marine engineering from the Northwestern Polytechnic University, Xi'an, China, in 1993, and the M.S. and Ph.D. degrees in electronic engineering from the National University of Defense Technology, Changsha, China, in 1996 and 2000, respectively.

He is an Associate Professor with the Remote Sensing Information Processing Laboratory, School of Electronic Science and Engineering, National University of Defense Technology. His research interests include SAR image processing, change detection, and classification with polarimetric SAR images.
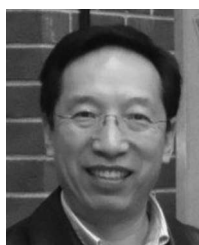
**Jonathan Li** (M'00–SM'11) received the Ph.D. degree in geomatics engineering from the University of Cape Town, Cape Town, South Africa.

He is currently with the MoE Key Laboratory of Underwater Acoustic Communication and Marine Information Technology, School of Information Science and Engineering, Xiamen University, Xiamen, China. He is heading Waterloo Laboratory for GeoSpatial Technology and Remote Sensing, Faculty of Environment, University of Waterloo, Waterloo, ON, Canada, where he is a Full Professor. He is the coauthor of more than 300 publications, around 100 of which were published in refereed journals. His research interests include information extraction from earth observation images and 3-D surface reconstruction from mobile LiDAR point clouds.

Dr. Li is a Chair of the Inter-Commission Working Group I/Va on Mobile Scanning and Imaging Systems of the International Society for Photogrammetry and Remote Sensing (2012–2016), a Vice Chair of the Commission on Hydrography of the International Federation of Surveyors (2015–2018), and a Vice Chair of the Commission on Mapping from Remote Sensor Imagery of the International Cartographic Association (2011–2015).

**Gang Chen** received the B.S. degree in geomatics engineering and the M.S. degree in photogrammetry and remote sensing from Wuhan University, Hubei, China, in 2003 and 2006, respectively, and the Ph.D. degree in geography from the University of Calgary, Calgary, AB, Canada, in 2011.

He is an Assistant Professor with the University of North Carolina at Charlotte, Charlotte, NC, USA. His research interests include the application of remote sensing, geospatial sciences, and machine learning to assess environmental change (with an emphasis on the dynamics of forest landscapes) in response to anthropogenic and natural disturbances.

Dr. Chen has published more than 20 peer-reviewed journal articles, and served as a reviewer for over 30 international journals, funding agencies and scientific conferences. He was the recipient of the 2011 Best Ph.D. Thesis Award from the Canadian Remote Sensing Society.
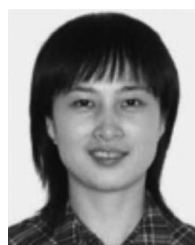
**Lingjun Zhao** received the B.S. degree in information engineering, the M.S. degree in circuits and system, and the Ph.D. degree in communication engineering from the National University of Defense Technology, Changsha, China, in 2003, 2004, and 2007, respectively.

She has been with the Remote Sensing Information Processing Laboratory, School of Electronic Science and Engineering, National University of Defense Technology, Changsha, China, since 2007. Her research interests include SAR image classification and urban SAR image interpretation, particularly automated extraction of urban objects (buildings, roads, etc.).

**Boli Xiong** (S'11–M'12) received the B.S. degree in electronic engineering, the M.S. degree in photogrammetry and remote sensing, and the Ph.D. degree in communication engineering from the National University of Defense Technology, Changsha, China, in 2004, 2006, and 2011, respectively

From 2008 to 2010, he was a Visiting Ph.D. student at the University of Toronto, Toronto, ON, Canada. He has been with the Remote Sensing Information Processing Laboratory, School of Electronic Science and Engineering, National University of Defense Technology, Changsha, China, since 2007. His research interests include synthetic aperture radar (SAR) information processing, forest tree height inversion with POL-interferometric SAR, and SAR image change detection.

**Gangyao Kuang** (M'11) received the B.S. and M.S. degrees from the Central South University of Technology, Changsha, China, in 1998 and 1991, respectively, and the Ph.D. degree from the National University of Defense Technology, Changsha, in 1995.

Currently, he is a Professor and Director of the Remote Sensing Information Processing Laboratory, School of Electronic Science and Engineering, National University of Defense Technology. His research interests include remote sensing, SAR image processing, change detection, SAR ground moving target indication, and classification with polarimetric SAR images.